

Synthetic photometry for carbon-rich giants

IV. An extensive grid of dynamic atmosphere and wind models ★★★

K. Eriksson¹, W. Nowotny², S. Höfner¹, B. Aringer², and A. Wachter³

¹ Department of Physics and Astronomy, Division of Astronomy and Space Physics, Uppsala University, Box 516, SE-75120 Uppsala, Sweden
e-mail: kjell.eriksson@physics.uu.se

² University of Vienna, Department of Astrophysics, Türkenschanzstraße 17, A-1180 Wien, Austria

³ Departamento de Astronomía de la Universidad de Guanajuato, Apartado Postal 144, C.P. 36000, Guanajuato, GTO, Mexico

Received; accepted

ABSTRACT

Context. The evolution and spectral properties of stars on the asymptotic giant branch (AGB) are significantly affected by mass loss through dusty stellar winds. Dynamic atmosphere and wind models are an essential tool for studying these evolved stars, both individually and as members of stellar populations, to understand their contribution to the integrated light and chemical evolution of galaxies.

Aims. This paper is part of a series with the purpose of testing state-of-the-art atmosphere and wind models of C-type AGB stars against observations, and making them available to the community for use in various theoretical and observational studies.

Methods. We have computed low-resolution spectra and photometry (in the wavelength range 0.35 – 25 μm) for a grid of 540 dynamic models with stellar parameters typical of solar-metallicity C-rich AGB stars and with a range of pulsation amplitudes. The models cover the dynamic atmosphere and dusty outflow (if present), assuming spherical symmetry, and taking opacities of gas-phase species and dust grains consistently into account. To characterize the time-dependent dynamic and photometric behaviour of the models in a concise way we defined a number of classes for models with and without winds.

Results. Comparisons with observed data in general show a quite satisfactory agreement for example regarding mass-loss rates vs. $(J-K)$ colours or K magnitudes vs. $(J-K)$ colours. Some exceptions from the good overall agreement, however, are found and attributed to the range of input parameters (e.g. relatively high carbon excesses) or intrinsic model assumptions (e.g. small particle limit for grain opacities).

Conclusions. While current results indicate that some changes in model assumptions and parameter ranges should be made in the future to bring certain synthetic observables into better agreement with observations, it seems unlikely that these pending improvements will significantly affect the mass-loss rates of the models.

Key words. stars: AGB and post-AGB – stars: atmospheres – stars: carbon – stars: variables: general – stars: mass-loss – circumstellar matter

1. Introduction

High luminosities, low effective temperatures and highly dynamic atmospheres are defining properties of AGB stars that make them popular targets for observations ranging from photometric monitoring to high-resolution spectroscopy and, more recently, NIR and MIR interferometry. They represent a crucial stage in the life of low- and intermediate-mass stars where mass loss is a decisive factor for the evolution, and newly produced chemical elements, most notably carbon, are fed into the surrounding ISM in the form of gas and dust by stellar winds. The production of new elements and their transport to the surface are the result of complex interlinked processes involving thermal pulses, hot bottom burning, and the third dredge-up (see, e.g. Herwig 2005; Karakas 2011; Stancliffe & Lattanzio 2011; Marigo et al. 2013). In addition to being interesting objects in

their own right, AGB stars are prominent members of stellar populations and important tools for extragalactic studies. All of these facts are good reasons for developing a better physical understanding of these stars, and a crucial part of that effort is the construction of detailed, realistic models of their atmospheres and winds.

This article is the fourth in a series dedicated to an in-depth analysis of synthetic observables, in particular, low-resolution spectra and photometry, resulting from state-of-the-art model atmospheres for carbon-rich giant stars. The first paper (Aringer et al. 2009, Paper I) presented a large grid of classical hydrostatic model atmospheres for C-type AGB stars, demonstrating that such models are applicable to the interpretation of objects with low pulsation amplitudes and very low mass-loss rates. For effective temperatures above 2800 K these models agree very well with observations. For cooler, more dynamic stars, however, the formation of dusty circumstellar envelopes severely affects the spectral energy distribution. The time-dependent effects of shock waves and dust formation on observable properties were discussed in detail in the second paper of this series (Nowotny et al. 2011, Paper II), based on one

* Appendices are only available in electronic form at <http://www.aanda.org>

** Table B.1, photometry and spectra for all snapshots are only available at the CDS. They can also be downloaded from <http://www.astro.uu.se/AGBmodels>

dynamic model with an intermediate mass-loss rate. The third paper (Nowotny et al. 2013, Paper III) extended the study of dynamic models to a small sample with stellar parameters representing different stages of AGB evolution, resulting in a sequence of increasing mass loss and correspondingly stronger circumstellar reprocessing of the photospheric fluxes. A detailed comparison with photometric observations of C-type AGB stars showed that our dynamic atmosphere and wind models reproduce a wide range of observed properties. References to other work based on hydrostatic and dynamic models can be found in Papers I and II, respectively.

In this paper we present results for 540 dynamic models, to a large extent based on the grid by Mattsson et al. (2010), to provide a consistent set of wind properties (mass-loss rates, outflow velocities, dust-to-gas ratios) and synthetic observables (low-resolution spectra, photometry) to the community. We discuss the influence of fundamental stellar parameters, pulsation properties, and certain model assumptions on the results, and compare them with various observations of carbon stars. This unique data set and accompanying information is made available in electronic form, providing input for theoretical studies on the evolution of individual stars and stellar populations, as well as for interpretations of observations.

Section 2 gives a short summary of modelling methods, described in more detail in earlier papers, and an overview of the physical parameters defining the model grid. In Sect. 3 we define classes characterizing the time-dependent dynamic and photometric behaviour of the individual models in a compact form (with representative examples discussed in Appendix A). In Sect. 4 we give an overview of the dynamic and photometric properties of the whole model grid, as well as a comparison with observations. Section 5 presents a brief summary and our main conclusions. Appendices B and C contain a short description of the material available at the CDS.

2. Dynamic models and radiative transfer

The modelling of dynamic structures and synthetic observables follows the approach described in Papers II and III of this series. Here we only give a brief summary, focusing on a few points of special interest, and referring to these and other papers for a more comprehensive description.

2.1. Dynamic atmosphere and wind models

The time-dependent structures of atmospheres and winds are produced by simultaneously solving the equations of hydrodynamics, frequency-dependent radiative transfer, and dust formation in spherical symmetry (cf. Höfner et al. 2003; Mattsson et al. 2010). The models cover two main dynamic aspects that affect the observable properties of AGB stars: pulsation-induced shock waves, and dust-driven winds (discussed in detail in Papers II and III). Each dynamic model is represented by a sequence of snapshots of radial structures, covering typically hundreds of pulsation periods.

The computations start from a hydrostatic, dust-free configuration characterized by the fundamental stellar parameters (mass, luminosity, effective temperature) and abundances of chemical elements, similar to classical model atmospheres. The effects of stellar pulsation are simulated by time-dependent boundary conditions at the inner edge of the computational domain, located just below the stellar photosphere. The velocity of the innermost mass shell is prescribed as a sinusoidal variation with period and amplitude as parameters (so-called piston

model), and the amplitude of the accompanying luminosity variation can be adjusted separately (see below).

Stellar pulsation – directly and indirectly – causes deviations from equilibrium at various scales. On the macroscopic level, propagating shock waves are triggered in the atmosphere, leading to extended, variable atmospheric structures that do not resemble hydrostatic atmospheres at any phase (Paper II, Nowotny et al. 2010). On microscopic scales, dust formation is proceeding far from equilibrium since the time scales for grain growth (involving the accumulation of $10^6 - 10^9$ atoms into a single grain) are similar to dynamic time-scales (Gustafsson & Höfner 2003). Therefore both phenomena, that is, gas dynamics (including shocks) and non-equilibrium grain growth, are described by detailed time-dependent equations in our models. Regarding even smaller scales, such as molecular chemistry, models presented for example by Cherchneff and collaborators (e.g. Cherchneff 2006, 2012) indicate that the effects of propagating shocks may drive the abundances of molecules away from their chemical equilibrium values. Including of full non-equilibrium chemistry in dynamic atmosphere and wind models, however, would considerably increase the computational effort and is therefore currently beyond the scope of large model grids. The effects of assuming molecular equilibrium in the gas phase when computing grain growth rates (as done here and in other dynamic models in the literature) is expected to be moderate in C-type AGB stars, since the growth of carbon grains can in principle proceed via a range of C-bearing molecules (or C atoms) and does not critically depend on a particular species.

2.2. Grid parameters

The stellar parameter combinations in the present grid correspond to a sub-sample of the radiation-hydrodynamic model grid presented by Mattsson et al. (2010, hereafter referred to as MWH10), with the constraint that they must be near the AGB tracks for solar-abundance evolution models, like those of Bertelli et al. (2008) or Marigo et al. (2008).

The models considered here have fundamental parameters (effective temperature, luminosity, and stellar mass) as given in Table 1. All models have solar abundances following Asplund et al. (2005), except for the carbon abundance. The values are given on the scale where $\log N_H \equiv 12.00$. The abundances from Asplund et al. (2005) correspond to a composition by mass, $X/Y/Z = 0.73/0.25/0.015-0.020$; the variation being due to the varying carbon abundance. For every combination of stellar parameters in the table, models were computed with carbon excesses of $\log(C-O) + 12 = 8.2, 8.5$ and 8.8 ¹ and with piston velocity amplitudes of $\Delta u_p = 2, 4$ and 6 km s^{-1} . The pulsation periods are given by the luminosity through a period-luminosity relation following Feast et al. (1989); for easy reference the periods are also given in Table 1 although they are not treated as an independent parameter.²

¹ The relation between the carbon excess, $\log(C-O)+12$, and the commonly used quantity C/O is given in Table 2. In contrast to other papers in the literature, we use the carbon excess to characterize the models because this quantity directly translates into the amount of carbon available for formation of carbon-bearing molecules (other than CO) and dust grains.

² The $P - L$ relation by Feast et al. (1989) is based on Miras in the LMC. In a diagram of K magnitudes vs. period as, e.g., in Ita et al. (2004), our models would largely overlap with the observed stars in sequence C. The stars belonging to this sequence are commonly believed to be fundamental-mode pulsators (Wood et al. 1999).

Table 1. Combinations of fundamental stellar parameters covered by the model grid. Note that the period is not an independent parameter but coupled to the stellar luminosity, see text. For each set of parameters listed here we varied the velocity and luminosity amplitude ($\Delta u_p, f_L$) of the inner boundary.

T_\star [K]	$\log L_\star$ [L_\odot]	P [d]	M_\star [M_\odot]	$\log(\text{C-O})+12$ [dex]
2600	3.70	294	0.75, 1.0	8.2, 8.5, 8.8
	3.85	390	0.75, 1.0, 1.5, 2.0	8.2, 8.5, 8.8
	4.00	525	1.0, 1.5, 2.0	8.2, 8.5, 8.8
2800	3.55	221	0.75	8.2, 8.5, 8.8
	3.70	294	0.75, 1.0	8.2, 8.5, 8.8
	3.85	390	0.75, 1.0, 1.5, 2.0	8.2, 8.5, 8.8
	4.00	525	1.0, 1.5, 2.0	8.2, 8.5, 8.8
3000	3.55	221	0.75	8.2, 8.5, 8.8
	3.70	294	0.75, 1.0	8.2, 8.5, 8.8
	3.85	390	0.75, 1.0, 1.5, 2.0	8.2, 8.5, 8.8
	4.00	525	1.5	8.2, 8.5, 8.8
3200	3.55	221	0.75	8.2, 8.5, 8.8
	3.70	294	0.75, 1.0	8.2, 8.5, 8.8

During a pulsation cycle the radius of the innermost mass shell of the model and the luminosity at that position vary simultaneously, simulating a coupling between the variable brightness and size of the star. Without a quantitative model of the pulsating stellar interior, assumptions have to be made about the forms, the amplitudes, and the relative phases of these temporal variations. Regarding the dynamic boundary (i.e. gas velocity), the functional form is of minor importance since the outward-travelling waves quickly develop into shocks, and the kinetic energy transferred into the atmosphere is mostly determined by the velocity amplitude. Therefore we adopted the common assumption of a sinusoidal variation, parameterized by the velocity amplitude Δu_p and the pulsation period P . For simplicity, we assumed that the luminosity at the position of the innermost mass shell varies in phase with its radius, and that the amplitude of the luminosity variation is correlated with the radius amplitude.

To avoid additional free parameters, we assumed in our earlier models (e.g. Höfner et al. 2003, MWH10) that the radius of the innermost model layer adjusts to the variable luminosity in such a way that the radiative flux is constant in time. This corresponds to the luminosity being proportional to the square of the radial position of the inner boundary. However, it turned out that this tends to give too small photometric variations compared with observations. Therefore we later generalized the description of the luminosity boundary condition to include an adjustable factor f_L , such that $f_L = 1$ reproduces the earlier results, and that the relative change in luminosity amplitude compared with that case is directly proportional to f_L (see, Nowotny et al. 2010, for details). In this study, we have varied the value of this parameter, using both the original value of $f_L = 1$ as in MWH10, and a newly calculated set of models with $f_L = 2$ (i.e. twice the luminosity amplitude of the original grid), these values are thought to bracket observed values (cf. Fig. 11). In addition, several of the original models from MWH10 were recalculated over a longer time interval to ascertain their long-term behaviour. In total, 540 different dynamic model atmospheres are used here (229 of them produced winds and 311 did not lead to outflows).

Table 2. Relation between the carbon excess measure $\log(\text{C-O})+12$ and the C/O ratio for the adopted chemical composition (Asplund et al. 2005), i.e. using an oxygen abundance of $\log(\text{N}_\text{O}/\text{N}_\text{H})+12 = 8.66$.

$\log(\text{C-O})+12$	C/O
8.2	1.35
8.5	1.69
8.8	2.38

2.3. Dynamic properties

The resulting dynamic properties of these models are compiled in Table B.1 The listed values are time-averages of the mass-loss rates, outflow velocities, and carbon condensation degrees, and were determined in the following way: for a given model, the existence of a wind was defined as the outer boundary having reached 25 stellar radii and the velocity of the gas at the outer boundary being positive (i.e. an outflow). Then, for each (pulsation) cycle with the wind condition fulfilled, the mass-loss rate etc. were determined and later means and standard deviations were calculated. For most models, several hundred cycles were used to determine the means (at least a hundred cycles for the non-episodic models).

In general, mass loss is favoured by low T_\star (easier to form dust at cooler temperatures), high luminosity (more momentum transferred from radiation to dust grains), small stellar mass (shallower potential well), large (C–O) (more free carbon to form amorphous carbon grains), and a large piston velocity amplitude (stellar layers reach out to a greater distance from the centre of the star).

2.4. Synthetic spectra and photometry

For each combination of input parameters, snapshots of the atmospheric structures at various phases (typically 20 per period), during several cycles (at least four) were used for the detailed *a posteriori* radiative transfer calculations. We applied our opacity generation code COMA (Aringer 2000, and Paper I) to compute atomic, molecular, and amorphous carbon (amC) dust opacities for all atmospheric layers and every wavelength point, assuming LTE. The dust opacity was calculated under the assumption of the small particle limit. Note that the treatment of the opacities is consistent with that in the generation of the dynamic models, except for a higher spectral resolution in the *a posteriori* radiative transfer calculations (10 000).

The resulting synthetic spectra in the wavelength range 0.35–25 μm were used to compute filter magnitudes in the Johnson-Cousins *BVR*I system (Bessell 1990) and the Johnson-Glass *JHKLL*'*M* system (Bessell & Brett 1988). More details can be found in previous articles, e.g. Paper II. The results given in Table B.1 include temporal mean of the *V* and *K* magnitudes, as well as their (maximum) ranges, and also the mean values of the colours (*V*–*I*), (*V*–*K*), (*J*–*H*) and (*H*–*K*). Data for the other computed filters, as well as spectra, for all computed phases are available in electronic form, see Appendix C.

3. Classes of dynamic and photometric behaviour

The dynamic response of the atmosphere to periodic driving by the piston and to outward acceleration by radiative pressure on dust can lead to a complex time-dependent behaviour of the models (including their photometric properties). This is because

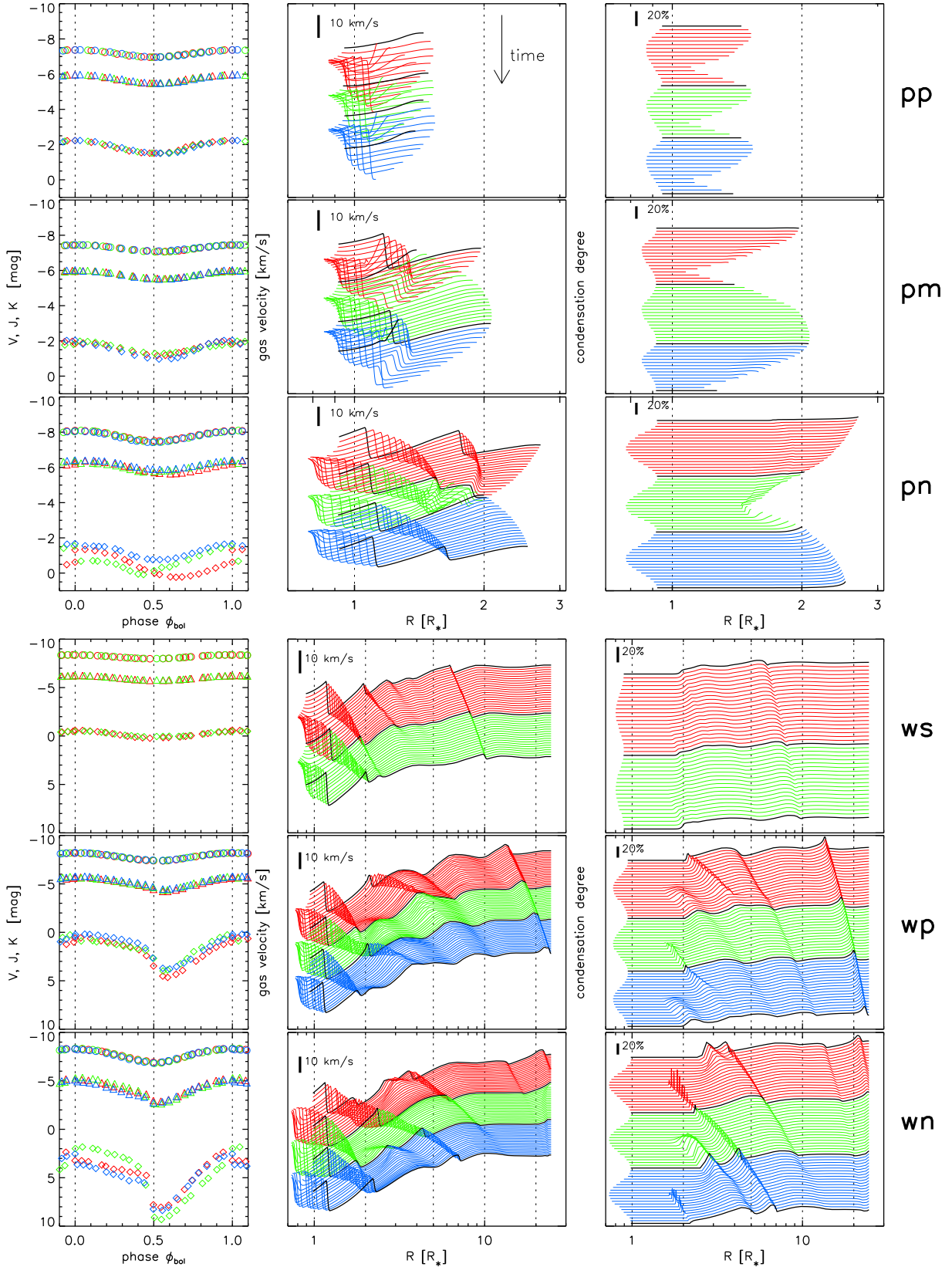


Fig. 1. Photometry and radial structures for representative models (see Table A.1) without wind (upper 3 rows, classes *pp*, *pm*, *pn*) and for models with winds (lower 3 rows, classes *ws*, *wp*, *wn*). The leftmost panels show the brightness in the *V* (diamonds), *J* (triangles) and *K* (circles) filters as a function of bolometric phase (with phase $\phi_{\text{bol}}=0.0$ at maximum light). Points belonging to the same pulsation cycle have the same colour. Note that the photometric scales are different for models with and without winds. Middle panels show radial profiles of the gas velocity. Each curve represents a snapshot in time, the first at the top and later ones displaced by a fixed amount downwards. The colours denote the different pulsation cycles and correspond to the colours in the leftmost panels. Black curves correspond to $\phi_{\text{bol}}=0.0$. Vertical dotted lines mark the distances 1, 2, 5, 10, and 20 stellar radii from the stellar centre. A velocity range of 10 km/s is marked with bars. The rightmost panels show radial profiles of the condensation degree of carbon plotted in the same way as the velocities, here the bars mark a condensation degree of 20%.

pulsation, atmospheric dynamics, and grain growth each have their own timescales. In Papers II and III of this series, we dealt with individual models where we could discuss the time-dependence of structures and observables in some detail. Here, we are faced with the challenge to characterize 540 models in a concise form, often with the use of temporal means of relevant quantities.

3.1. Definition of classes and examples

In this section, we define classes as a simple shorthand notation for describing the time-dependent (dynamic and photometric) behaviour of the models. The models without a wind are divided into the classes *pp*, *pm*, and *pn* (with the first letter *p* denoting “pulsating atmosphere”). The *pp* models are regularly *periodically pulsating*, repeating their dynamic behaviour every period. In the *pm* class we put models that repeat after two (sometimes more) periods (*pulsating, multi-periodic*). Other, more irregular models, are put in the class *pn* (pulsating, non-periodic). Models with winds are similarly divided into the classes *ws*, *wp*, and *wn* (with the first letter *w* denoting “wind”). Here the *ws* class includes models with a *steady* wind with small temporal variations in mass-loss rates and wind velocities. The models in the *wp* class show *periodic* variations in the wind properties, while the *wn* class includes models with more irregular behaviour (*non-periodic*). Finally, a transition class *we* contains the *episodic* models, that is, models that show an intermittent outflow.

The time-dependent behaviour of the different classes (except *we*) is illustrated in Fig. 1 for representative models. The middle and right panels in the figure show radial profiles of the gas velocity and the condensation-degree for carbon, respectively. Each curve represents a snapshot in time, with time running downwards and with different colours to denote different stellar pulsation cycles. The panels in the left column display light curves as a function of phase (with phase $\phi_{\text{bol}}=0.0$ at maximum light) in the photometric *V*, *J* and *K* filters (with the colour of the symbols denoting the different cycles). Information on which specific models were chosen as representative cases, and more details about them can be found in Appendix A.

It should be pointed out that dust formation is a necessary but not a sufficient condition for the development of a wind, and even for the models without a wind the presence of dust can be important (see Fig. 1, the *pn* case). Photometrically, the amC dust opacity, being roughly inversely proportional to the wavelength, will extinct the visual light much more than, for example, the near-IR radiation, and for light with wavelengths longer than $\sim 2\mu\text{m}$ the dust emission will dominate absorption.

For the models without a wind in Fig. 1 (upper 3 panels) we see that even very small amounts of dust (corresponding to condensation degrees of the order of a few per mille of carbon atoms) will noticeably affect the *V* light-curve (e.g. the *pm* model), and that the position in time of minimum light depends on where and when the dust formation takes place (e.g. the *pn* model), especially for the *V* filter. The photometric behaviour of wind models (Fig. 1, lower 3 panels) is also clearly related to dust formation. The outward-moving shocks with enhanced dust are quite noticeable. Moreover, the *V* magnitude behaviour is clearly related to the amount of dust formed at 1.5 – 2 stellar radii around the luminosity minima. Many models in class *ws* produce much dust, with a rather large but almost constant condensation degree of carbon. These models then show comparatively small variations in the *V* magnitude. Finally, we find examples of models with photometric behaviour in *V* that suggest a different period than that of the piston. An example is

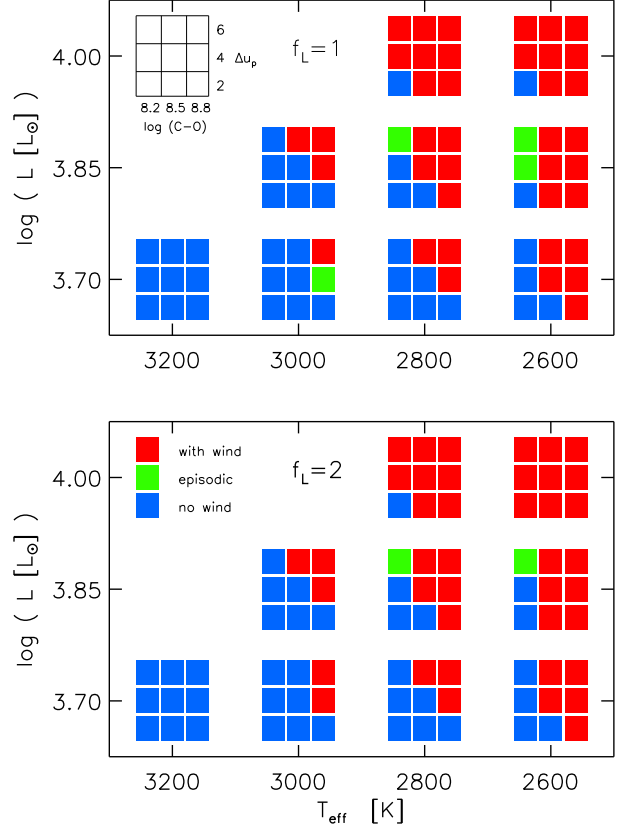


Fig. 2. Schematic overview showing the dynamic behaviour of the $1 M_{\odot}$ models as a function of other model parameters. Note that the temperature increases to the left in a format resembling an HR-diagram.

given in Fig. C.1, where we see that one could derive a period from the *V* magnitudes that is twice the luminosity period (or the one derived from *K* magnitudes). Another example of this behaviour, illustrated with detailed plots, can be found in Paper III, Appendix C. So again we see the importance of dust formation for the photometric behaviour in the visual wavelength region.³

One model shows unusual photometric properties for its class. It has the parameters $T_{\star} = 2600\text{ K}$, $\log L = 3.70$, one solar mass, $\log(\text{C-O})+12 = 8.2$, $\Delta u_p = 6$, and $f_L = 2$ and belongs to the *pn* class. The effective temperature is low but the luminosity and/or carbon excess is not high enough to initiate even a marginal wind. Instead, the model consists of a dusty outer atmosphere that extends to 5–10 stellar radii and with a high carbon condensation degree of 40–80%. Therefore, it is found in positions unexpected for its class in colour-magnitude and two-colour diagrams (Figs. 12 and 13).

3.2. Trends with model parameters

The different kinds of dynamic behaviour can be understood relation to the model parameters as follows.

First, for a given combination of stellar mass, luminosity and effective temperature, we note that with increasing value for the piston velocity amplitude ($\Delta u_p = 2 \rightarrow 4 \rightarrow 6 \text{ km s}^{-1}$) the outer stellar atmosphere will ballistically expand to increasing greater heights. After reaching the maximum height, the downward moving gas will, at some height, encounter the outward moving gas in the next pulsation cycle. Depending on when this occurs, we see different scenarios: from cases where the whole atmosphere moves together in phase with the pulsation, situations where the outgoing shock wave interacts with downward falling material in complex ways. So, we have cases from the *pp* class (where the behaviour repeats each period) over the *pm* class (with a repetition after two or more periods), to the *pn* class with a more irregular behaviour. If the outward moving gas becomes cool and dense enough to allow dust formation, this will affect both the dynamic and photometric behaviour. Dynamically, the additional momentum given to material through the radiative acceleration of the dust and then to the gas via the collisional coupling. If the radiative acceleration exceeds the gravitational one, a stellar wind will form. We find that, when dust formation occurs around 1.5 – 2 stellar radii (from the stellar centre and outwards). Depending on how much dust forms and where it forms, we find different kinds of wind classes: for the *ws* class we see small variations of the degree of carbon condensation into dust at the same distance, for models in the *wp* class dust formation occurs in a regular way (similar amounts of dust at similar distance every cycle or in a periodic pattern), and for the *wn* class models the amounts and positions of dust formed vary in a more irregular way.

Second, for a given combination of stellar mass, luminosity and effective temperature, we find that with increasing carbon excess ($\log(\text{C-O})+12 = 8.2 \rightarrow 8.5 \rightarrow 8.8$) the dust-to-gas ratio increases: a high carbon excess facilitates the formation of a wind (and, as we will see, also increases the terminal wind velocity through increased radiative acceleration), as well as increasing the effects of dust on the photometry.

The behaviour as a function of stellar mass, luminosity and effective temperature can be understood in the following way: (i) dust formation is favoured by a lower temperature, and (ii) a higher luminosity or a lower stellar mass will help the radiative acceleration on dust to overcome the stellar gravity. A schematic representation of the occurrence of stellar winds for $1 M_\odot$ models is given in a format like an HR-diagram in Fig. 2, illustrating the trends discussed above.

The parameter f_L , discussed in Sect. 2.2, regulates the luminosity amplitude of the model without changing the kinetic energy input due to pulsation (which is determined by Δu_p and P). Figure 3 where the distribution of our models over the different classes is shown, separately for the different f_L values, gives a first indication that the effect of f_L on the dynamics and wind properties is minor. The two cases give similar distributions, the only possibly significant difference between $f_L = 1$ and $f_L = 2$

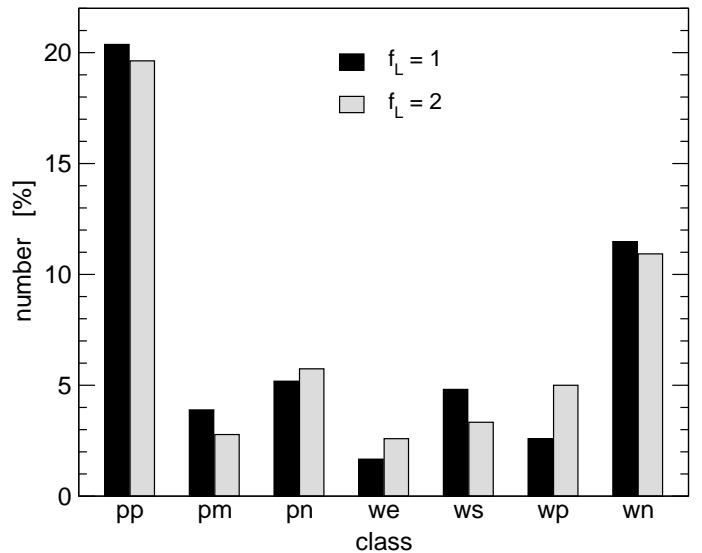


Fig. 3. Distribution of models over classes of time-dependent behaviour, shown separately for the two values of f_L .

being that the relative numbers of models in the classes *wp* and *ws* change. We further discuss the effects of f_L in a more quantitative way in Sect. 4.1.

4. Overall properties of the model grid

After looking into representative examples of time-dependent behaviour we now discuss the model grid as a whole, that is, trends of resulting properties with input parameters and how our group of models compares to observational samples. As mentioned in Sect. 2.2, the present grid parameters form a sub-sample of the original grid range of MWH10. They cover the region where most carbon-star models appear in synthetic stellar evolution calculations for solar metal abundances (e.g. those of Bertelli et al. (2008) or Marigo et al. (2008)).

Directly from the radiation hydrodynamic calculations we obtain the mean mass-loss rates, wind velocities, carbon condensation degrees, and dust-to-gas ratios as well as their standard deviations (everything computed at the outer boundary at 25 stellar radii, see Sect. 2.3). The *a posteriori* radiative transfer calculations give us the mean photometric magnitudes and their variations in different filters (cf. Sect. 2.4). Here we restrict the discussion to temporal means of all values (usually taken over several hundreds of periods).

When we compare the results from the present calculations with data from various observational samples of carbon stars, it is important to bear in mind that all parameter combinations get the same weight in our grid, whereas in the observational samples the number of targets with corresponding stellar parameters will depend on the initial mass function, stellar evolution effects, observational selection criteria, etc.

In this section we first discuss the dynamic properties of the grid and then present the photometric results from the radiative transfer calculations.

4.1. Wind properties

Mass-loss rates and outflow velocities are two essential wind properties, and are also direct results of the dynamic models. In Fig. 4 (upper panel) we show a comparison of these quantities with empirical data adopted from the literature. The dependence

³ It is interesting to speculate if this behavior (i.e. a dust formation cycle corresponding to two pulsation periods) explains observed stars lining up along Sequence D in a K magnitude vs. period diagram (e.g. Ita et al. 2004), with K magnitude unaffected but observed periods corresponding to twice the fundamental mode pulsation. However, we would like to defer a discussion of this point to a future paper since current synthetic V light curves are affected by the assumption of small particle limit for grain opacities.

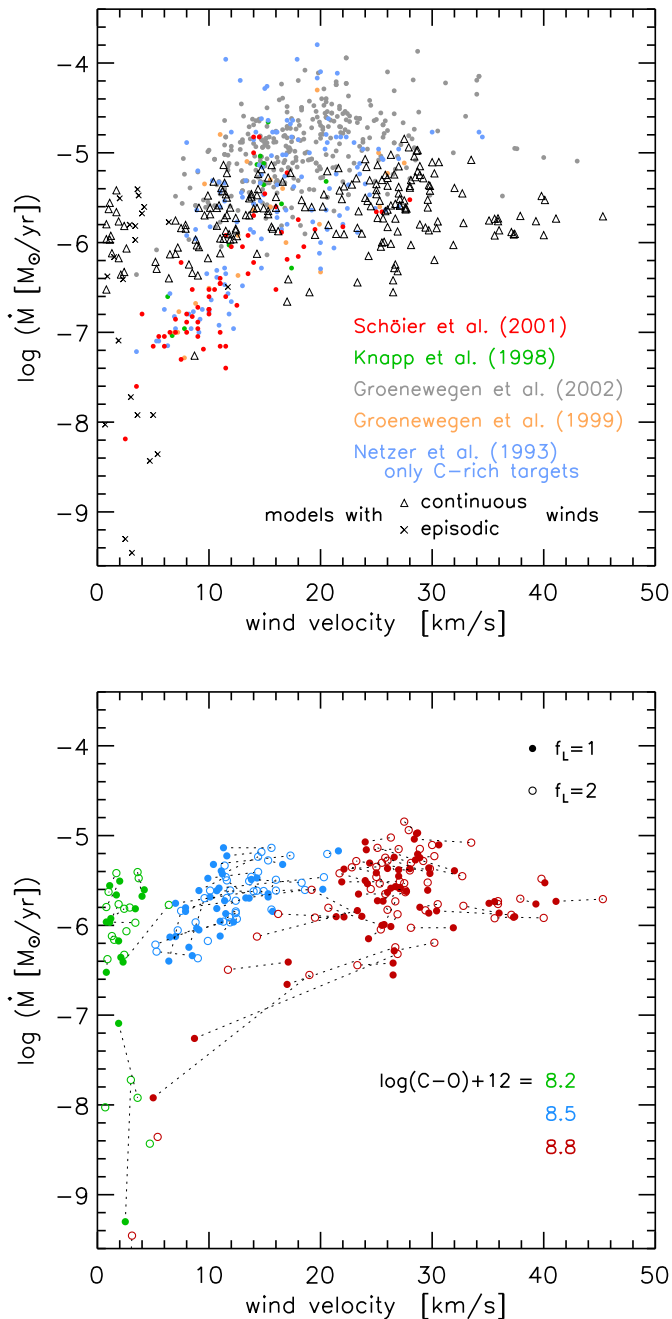


Fig. 4. Mass-loss rate plotted versus the wind velocity for all models with outflows. In the upper panel the triangles mark models with steady winds while the crosses denote models with episodic winds. The other symbols with different colours show values based on observations of various C-rich giants, adopted from different sources as given by the legend. The lower panel shows the values for the models which have winds for both $f_L = 1$ and $f_L = 2$. The latter are plotted as open circles and models with identical parameters except f_L are connected. The different colours denote various carbon excesses.

of model properties on carbon excess and luminosity amplitude is shown in the lower panel: in the current grid there are 229 models, i.e. 42% of the models, that give outflows. In general, the wind models fall nicely within the region covered by observed stars. However, there is one noticeable exception: a group of models with very low wind speeds and relatively high mass-loss rates, corresponding to the lowest $\log(\text{C}-\text{O})+12$ value (8.2), which have no counterparts among the observed stars. These

models can probably be brought into better agreement with observations by giving up the small-particle limit assumption when computing grain opacities (used for keeping the models comparable to MWH10). An exploratory study by Mattsson & Höfner (2011) demonstrated that the outflow speeds for models with relatively slow winds tend to increase considerably when using proper size-dependent grain opacities while the mass-loss rates are largely unaffected (see the second column of Fig. 4 in their paper). This effect is due to a higher efficiency factor for grains with radii of a few tenths of a micron (see Fig. 3 in Mattsson & Höfner 2011) and would most likely shift the group of low carbon excess models to the right in Fig. 4 (note that there seems to be little or no effect on models with wind velocities higher than 10 km s^{-1} with small-particle limit opacities).

As already stated in MWH10, we note a lack of models with low mass-loss rates, except for a few cases with episodic winds. We also note in Fig. 4 that some models with $\log(\text{C}-\text{O})+12 = 8.8$ show higher wind velocities than the bulk of the observed stars, probably indicating that such high carbon abundances are rare. Furthermore, the current model grid does not cover objects with the highest mass-loss rates derived for instance by Groenewegen et al. (2002) or Netzer & Elitzur (1993). This might be due to the selected physical parameters or uncertainties in the empirical mass-loss rates.

For the comparisons with empirical data it should be kept in mind that mass-loss rates are direct results of the models, whereas they may be less straightforward to derive from observations, depending on the type and quality of data, as well as the methods of interpretation.⁴ Ramstedt et al. (2008) concluded that the mass-loss rates in Schöier & Olofsson (2001) are reliable within a factor of three. Values derived with other methods are probably less accurate. For the empirical data shown in Fig. 4 we checked that for stars that appear in more than one sample, the derived mass-loss rates do not deviate significantly from the values given by Schöier & Olofsson (2001).

We now examine the role of the parameter f_L , which was introduced to bring the light curve amplitudes into better agreement with observations without changing the input of kinetic energy due to pulsation (see Sect. 2.2). In the grid by MWH10 this parameter was held constant at $f_L = 1$. We find that the dynamic effects of changing this parameter are minor, while the effects on the photometric variations are quite pronounced. In Fig. 4 we see that when f_L is increased from 1 to 2, the mass-loss rates are basically unchanged (except for marginal winds, i.e. low mass-loss rates) and that changes in the outflow velocity go both ways although a velocity increase is slightly more common ($\sim 60\%$). Therefore, we conclude that it should be safe to use the mass-loss rates from the MWH10 grid for example in stellar evolution calculations.

Mattsson et al. (2010) studied the dynamic properties as a function of a quantity α , defined there as $(\rho_d/\rho_g)(L_{\star}/M_{\star})$, which is proportional to the ratio of radiative to gravitational acceleration. As discussed there, one expects that the outflow velocities are more directly correlated with α than the mass-loss rates. In the upper panel of Fig. 5 we plot the outflow velocities vs. α for our grid, where the different dynamic classes are marked. Excepting episodic models, we see a relatively narrow relation up to about an outflow velocity of 20 km s^{-1} , and a tendency

⁴ On the other hand, certain directly observable quantities may not put strong constraints on the dynamic models if they measure parameters that have little influence on the resulting model properties (see Sect. 4.2). Often, comparisons are therefore a trade-off between direct accessibility and relevance of the information, and the choice of quantities to be compared between models and observations is non-trivial.

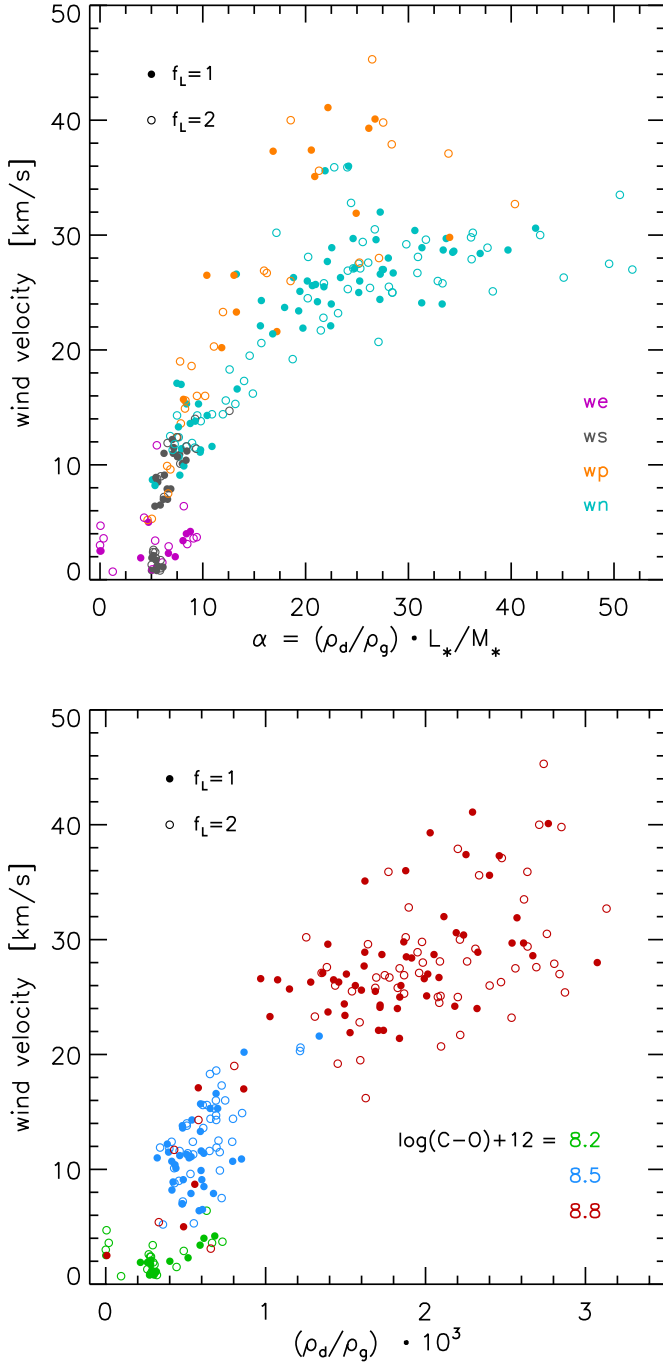


Fig. 5. The terminal wind velocities as a function of α (upper panel) and as a function of the dust-to-gas ratio (lower panel) for all models developing outflows.

for a separation for higher velocities such that the class *wp* continues the steeper trend and for other classes the increase with α is much slower, leveling off at a terminal velocity around 30 km s^{-1} . The reason could be a constructive resonance between dust formation and radiative acceleration for the *wp* class models (since the radiative acceleration of the dust varies with time as the luminosity). Note that the corresponding figure in MWH10 looks different because of their selection of stellar parameters (they also included models with $\log L = 4.15$ and $\log(\text{C-O})+12 = 9.1$), and because they did not have any models with $f_L = 2$.

To separate the effect of the dust-to-gas ratio on the outflow velocities from the influence of stellar parameters, see also the

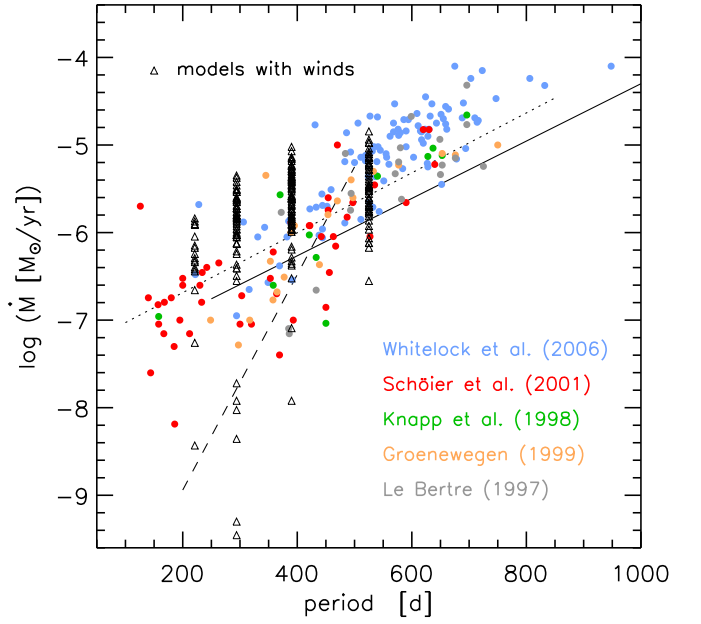


Fig. 6. Mass-loss rate as a function of pulsation period for the models with winds, plotted as black triangles compared to observations of various galactic C-rich targets from various sources. The plotted relations come from Vassiliadis & Wood (1993) (dashed line), Groenewegen et al. (1998) (their Eq. 9, C-miras; solid line), and De Beck et al. (2010) (fit on their page 21; dotted line).

lower panel of Fig. 5. The range in α is mainly a range in (ρ_d/ρ_g) as (L_*/M_*) only varies by a factor of about three for the models. The figure shows that the outflow velocity dependence on the (ρ_d/ρ_g) ratio largely is an effect of the carbon excesses (as a large carbon excess favours the condensation of amorphous carbon dust and consequently facilitates the acceleration of gas and dust). The variation of the (ρ_d/ρ_g) ratio by a factor of 30 or more found in the models makes it questionable if the commonly used assumption of a constant (ρ_d/ρ_g) value when deriving mass-loss rates from observations is justified.

The mass-loss rates derived from several observational studies are plotted against observed periods in Fig. 6 and are compared to the models. As mentioned above, the pulsation periods for our models are taken from an adopted period-luminosity relation. We see here that the slopes of the mass-loss rate vs. period relation from our computations are fairly consistent with the empirical relations by Groenewegen et al. (1998) and De Beck et al. (2010). The relation from Vassiliadis & Wood (1993) seems too steep, again bearing in mind that our grid does not correspond to a stellar population. The computed mass-loss rates for the models with the shortest periods (i.e. lowest luminosities) are higher than those for most observed short-period AGB stars (these models usually have high carbon excess and large piston amplitudes and have no observed counterparts in this plot).

Finally, in Fig. 7, we also compare our model grid with the mass loss formula given by Wachter et al. (2002), based on an older generation of dust-driven wind models. The mass-loss rates resulting from our models are systematically, and often significantly, lower than the values obtained from the mass-loss formula for the same stellar parameters. The main physical difference between the two sets of models is the treatment of gas opacities and radiative transfer. In contrast to the dynamical models discussed here (which include frequency-dependent radiative

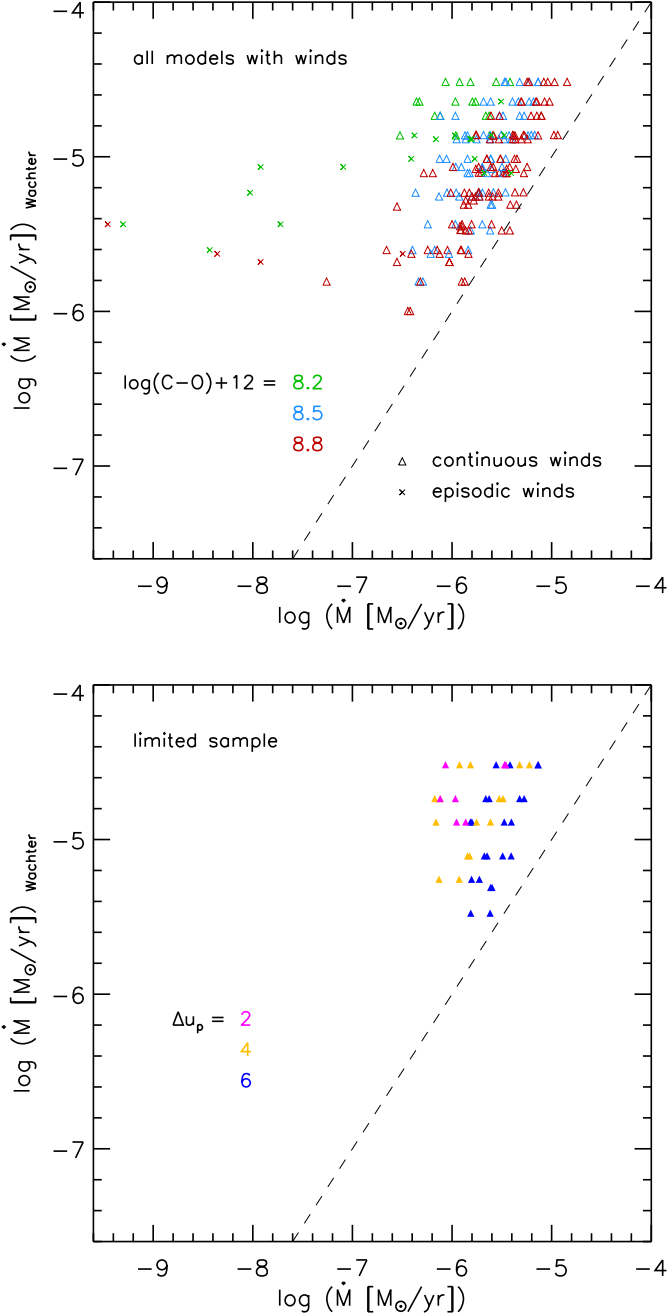


Fig. 7. Comparison of the mass-loss rates for the present model grid with the values computed from the mass-loss rate formula of Wachter et al. (2002) using the same stellar parameters. The top panel shows the result for all models with winds, while the lower panel shows it for a subsample of models that fall within the range for which the formula was originally derived ($\log(\text{C-O})+12 = 8.2$ and 8.5 and one solar mass). The systematic differences are due to differences in the underlying models, see text.

transfer with detailed gas and dust opacities, see Sect. 2.1), the models used by Wachter et al. (2002) are based on grey radiative transfer with a constant value of the gas opacity. This affects the density-temperature structures of the atmospheres in a decisive way: the low value chosen for the gas opacity in the model set used by Wachter et al. (2002) results in much higher gas densities at a given temperature, translating into systematic differences in mass-loss rates. A strength of the present model grid, resulting from its more realistic input physics, is that synthetic

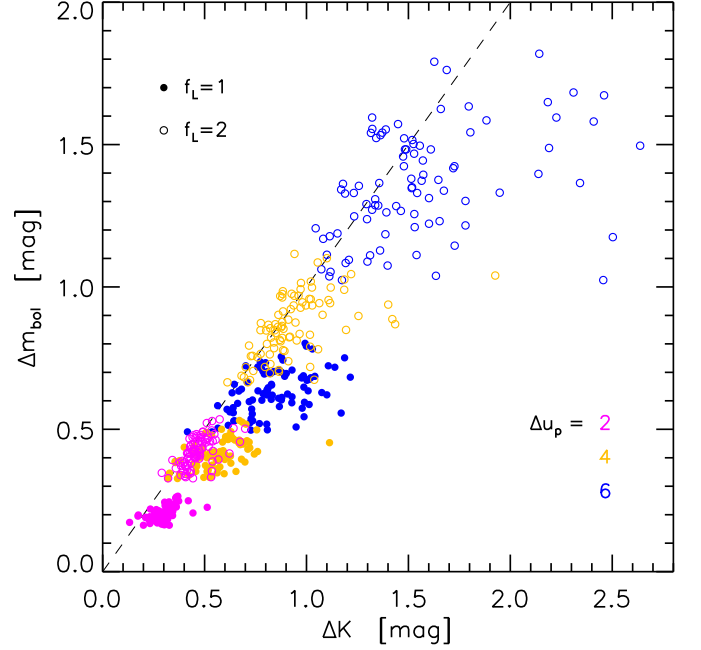


Fig. 8. Correlation between the bolometric amplitudes, Δm_{bol} , and the amplitude in K , ΔK , for the grid models. The dashed line is the 1:1-line.

observables such as photometric colours compare quite well with observations, as is discussed in the following section. Therefore, we conclude that using the formula by Wachter et al. (2002) in stellar evolution models probably leads to an overestimation of the mass-loss. For a discussion why we have not given a new formula based on the current grid, see Sect. 4.5 of Mattsson et al. (2010).

4.2. Photometric properties

The spectra from the inner atmospheres are dominated by the usual molecular features found in cool carbon stars – CO, C_2 , CN, HCN, C_2H_2 , etc. If dust is formed farther out, the spectra are modified by the amC grain opacity, attenuating the visual spectra and adding dust emission for wavelengths $\gtrsim 2\mu\text{m}$. This was discussed in some detail in Papers II and III. In particular, the effects of the dust opacity for different photometric filters are discussed and shown in Fig. 3 of Paper III.

In short, the K magnitude is a good proxy of the luminosity (K being a filter where the dust extinction and emission nearly balance each other, see Fig. 4 in Paper II), and thus ΔK is a measure of luminosity variations. This is illustrated in Fig. 8, where these two quantities are plotted against each other and most of the models are located close to the 1:1-line. Models with significantly larger ΔK correspond to heavily enshrouded objects where the entire SED is shifted towards longer wavelengths.

In contrast to the K band, the J filter is more affected by dust extinction, so the $(J-K)$ colour will mostly be a measure of the importance of dust extinction in the atmosphere/wind regions (apart from the obvious T_\star dependence). In the following we describe how the photometric properties (i.e. amplitudes in various filters, mean colour indices) vary across our grid of models and how they compare to observations.

As the main observational reference we used the compilation of time-series, near-infrared (NIR) photometry published by Whitelock et al. (2006; below W06). They presented comprehensive data sets for a large sample of Galactic carbon-rich

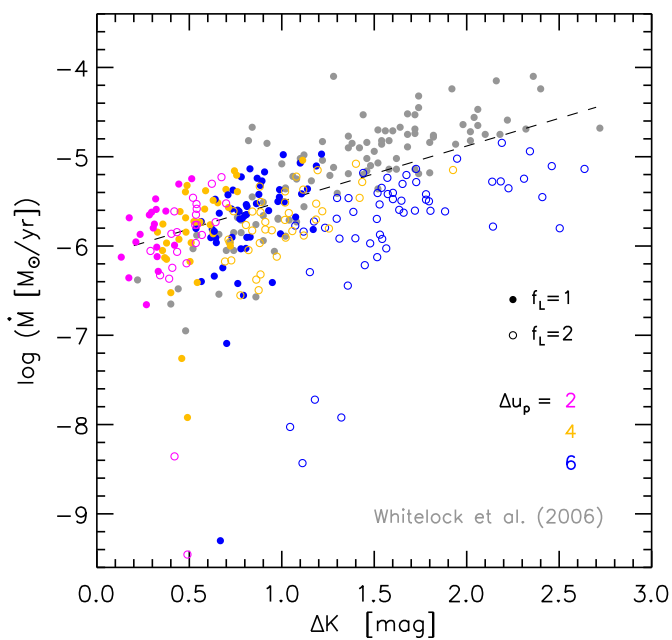


Fig. 9. Mass-loss rates as a function of the K amplitude of the models, as well as for observed stars in W06 (grey dots). The dashed line is a fit for carbon miras from Groenewegen et al. (1998), Eq. 11.

AGB stars. Here we adopted the results for their sub-sample of well-characterized Mira variables (cf. Paper III).

A comparison of the mass-loss rates as a function of the K amplitudes is shown in Fig. 9 for the models developing winds and for observational results taken from Whitelock et al. (2006), hereafter often referred to as W06. This is our main observational reference where time-series of NIR photometry for Galactic carbon-rich AGB stars are presented. We note in Fig. 9 that the inferred very high mass-loss rates ($> 10^{-5} M_{\odot} \text{yr}^{-1}$) for many (mostly distant, very red) stars have no counterparts among the models in our grid. It is also evident from the figure that our models show a significant spread in mass-loss rate for given ΔK . In this context, we recall that ΔK is, in essence, a measure of the luminosity amplitude, and that we showed earlier that this quantity *per se* (i.e. as far as it is not a consequence of a higher piston velocity amplitude but only an effect of f_L) has very little influence on the dynamics and mass-loss rate (see Figs. 3 and 4). With other stellar parameters not constrained, and no underlying pulsation model (giving an intrinsic coupling between the amplitudes of velocity and luminosity at sub-photospheric layers) a tight correlation between mass-loss rate and ΔK in the models is therefore not expected.

How do the mass-loss rates of the models as a function of the calculated mean $(J-K)$ colour compare with the corresponding observed/derived quantities for AGB stars? In Fig. 10 we see that the models and observations show a similar trend and that the models cover most of the space occupied by observed data from Whitelock et al. (2006). When considering the distribution of models in this diagram, one must bear in mind that the relative weights of parameters for the model grid do not correspond to those of an observed sample.

The clear correlation of mass-loss rate and $(J-K)$ seen in Fig. 10 for both models and observations is a demonstration of the fact that this colour is a good proxy for the optical depth of the circumstellar envelope. At a closer look, however, the good quantitative agreement between models and observations is difficult to understand, considering the fact that the empirical values

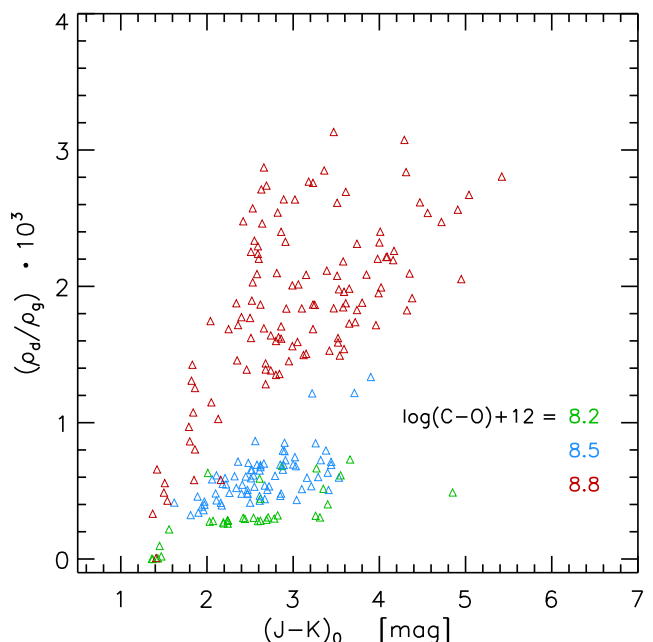
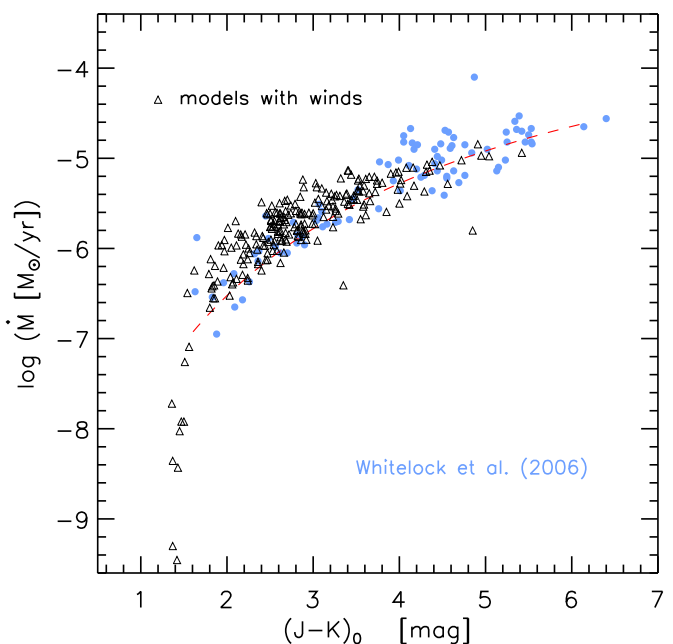


Fig. 10. Upper panel: mass-loss rate as a function of mean $(J-K)$ colour for models and observed stars. The dashed line is a fit from Gullieuszik et al. (2012) for LMC carbon stars, the values derived by W06 are plotted as blue dots. The lower panel shows the dust-to-gas ratio as a function of the mean $(J-K)$ colour for the models.

of W06 are based on the assumption of a constant, rather high dust-to-gas ratio that disagrees with the model results (see lower panel of Fig. 10).⁵ The clear discrepancies in the dust-to-gas ratio must be compensated for by other assumptions underlying the empirical data and/or the models to arrive at the good agreement in the correlation between mass-loss rate and $(J-K)$.

⁵ The observed mass-loss rates, in e.g. W06, are derived from the measured IRAS $60 \mu\text{m}$ flux, involving estimated distances (squared) and a fixed dust-to-gas ratio. This value is commonly assumed to be around 0.005 (Gullieuszik et al. 2012, W06, based on Jura (1987)), which is systematically higher than in our models.

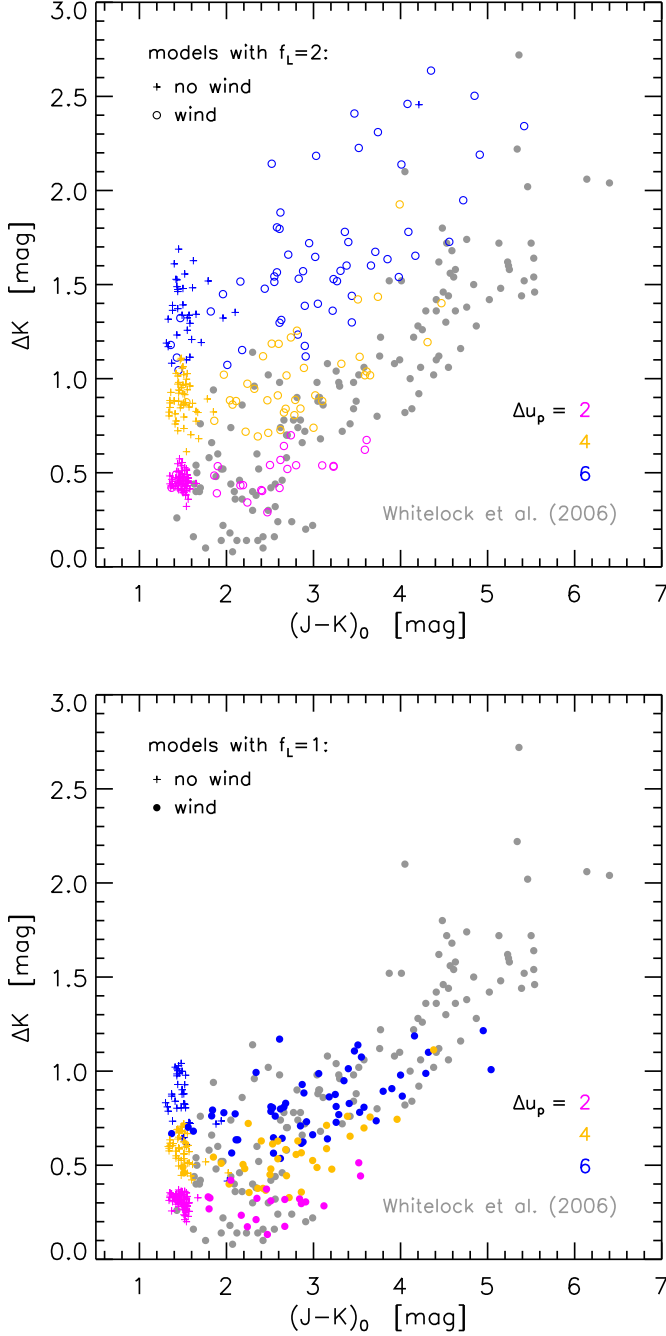


Fig. 11. The amplitude of the K -magnitude variations vs. mean $(J-K)$ for the grid models and observed values from W06 (grey dots). The upper panel shows the $f_L=2$ models, and the lower one the $f_L=1$ ones.

A way to avoid the uncertainties in the mass-loss rates derived from observations is to compare synthetic observables of the dynamic models with directly observed quantities. A rather easily obtained observable is the amplitude in the K magnitude, ΔK . The computed values of ΔK as a function of the mean $(J-K)$ colour are displayed in Fig. 11 together with observational data from W06. Since ΔK is a measure of the luminosity variations and both f_L and Δu_p have an influence on the luminosity amplitude, we split this figure into panels for the two differ-

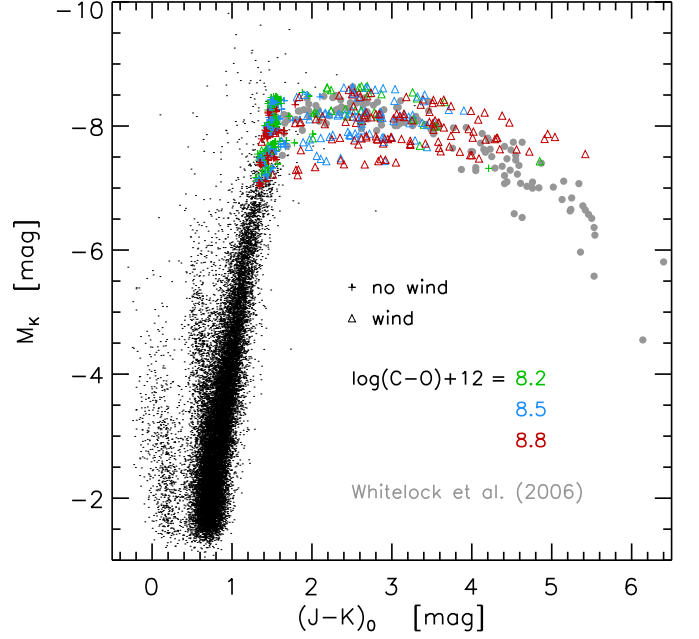


Fig. 12. Colour-magnitude diagram showing K -magnitudes vs. mean $(J-K)$ for the grid models together with the observed sample of W06 and 2MASS data for Baade’s window (see Paper III for a detailed description).

ent f_L values and show the Δu_p values in different colours.⁶ The plotted value of ΔK is the mean of the amplitudes in K for all selected cycles (i.e. at least four), whereas the $(J-K)$ value is the temporal mean of this colour. We see that the models with $f_L=2$ and the largest piston amplitude have photometric colours that are rarely observed for carbon stars. Note also the clear dependence of ΔK on the piston amplitude, as well as the fact that wind models and those without a wind have approximately the same ΔK for a given Δu_p (except for models with $f_L=2$ and a very substantial wind, i.e. large $(J-K)$). In Paper III (their Fig. 11) it was illustrated that $(J-K) \sim 1.6$ marks the border between the models with and without winds; here we see that also for the present grid a $(J-K)$ value of around 1.7 marks this division.

In Fig. 12, showing a colour-magnitude diagram, we compare K magnitude values from the models with observations in Baade’s window and from W06. These data were discussed in Paper III. Here the model values also cover most of the space occupied by the observed giant stars, except for the reddest objects. We note that models with some of our chosen parameters have no counterparts among the observed stars, especially the low-mass, low-luminosity models that have large enough carbon excess and piston velocity amplitudes to initiate a wind. As we already noted, the latter group also deviates from observations in Fig. 6.

In the commonly used $(J-H)$ vs. $(H-K)$ plot, shown in Fig. 13, we note a general agreement between model colours and observed ones for models with a substantial wind. The red $(J-H)$ and $(H-K)$ colours are due to dust (for details see Paper III, Sect. 5.2). For the wind-less models we note that they appear “too blue” in $(J-H)$ and/or “too red” in $(H-K)$ compared with the observed samples. It is interesting to note that hydrostatic models that are computed with still smaller carbon

⁶ Note that while both parameters affect the luminosity amplitude, the different Δu_p also correspond to different inputs of kinetic energy at the inner boundary, which is not the case for f_L , cf. Sect 2.2.

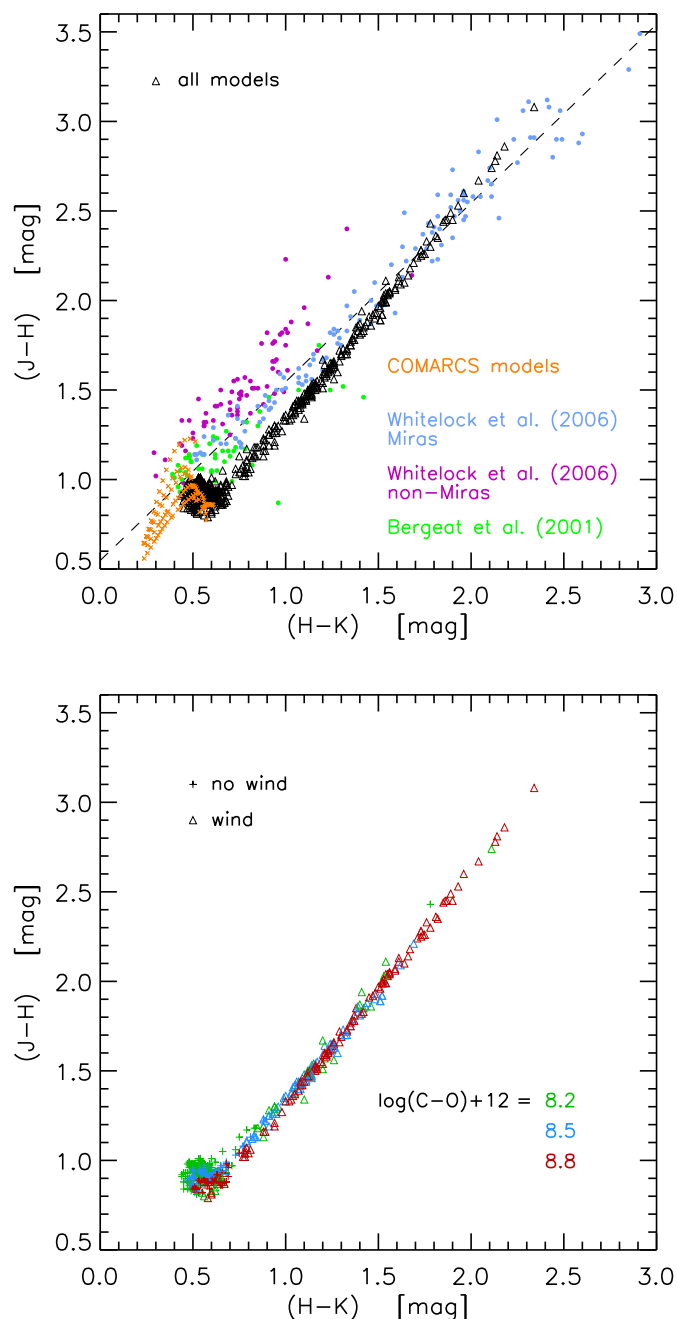


Fig. 13. Mean $(J-H)$ colour vs. mean $(H-K)$ for the model grid and some observed samples. The fit in the upper panel comes from W06, Eq. 2. We also plot values for hydrostatic COMARCS models with low $(C-O)$, see text.

excesses (corresponding to C/O ratios around 1.1, Paper I) do fall around $(H-K), (J-H) \simeq (0.4, 1.1)$ – for these stars the dynamic effects are expected to be small.

5. Summary and conclusions

The results presented in this paper are based on state-of-the-art atmosphere and wind models of carbon stars, spanning a considerable range in fundamental stellar parameters (given in Table 1) with three values of carbon excess, three values of piston velocity amplitude, and two values of the parameter f_L defining the luminosity amplitude. For these 540 models, we per-

formed *a posteriori* radiative transfer calculations for representative snapshots of structures, covering wavelengths from 0.35 to 25 μm . We considered opacities from gas (atomic and molecular lines, continuous sources) as well as from amorphous carbon dust grains (when present). The results are available for down-loading and include dynamic properties (mass-loss rates, outflow velocities, dust condensation degrees) as well as spectra and photometric quantities. The data, especially the mass-loss rates, can be used in stellar evolution modeling, or for population synthesis where photometric properties are needed. Another possibility is to study individual carbon stars using these data.

When comparing our results with observed quantities for individual or samples of carbon stars, several aspects must be kept in mind. First we have the intrinsic limitations and assumptions in the models, such as neglecting 3D effects by assuming spherical symmetry, and using the small-particle limit for grain opacities. Second, certain parameter choices for the current modelling, such as the velocity and luminosity amplitudes, are proxies for a more realistic treatment of the pulsational behaviour of real AGB stars. Third, our grid contains models regardless of how common a particular parameter combination would be in a real stellar population, characterized by an initial mass function, age, and metallicity distribution, and modified by stellar evolution.

Despite these caveats, we see, in general, a rather satisfactory agreement of typical models with representative stars, regarding both dynamic and photometric properties, such as mass-loss rates vs. $(J-K)$ colours, K magnitudes vs. $(J-K)$ colours, and the colour-colour diagram of $(J-H)$ vs. $(H-K)$ (the latter with the exception of models with small or no mass-loss; probably an effect of lacking low $(C-O)$ values in the current grid). This is in line with our earlier detailed comparisons of selected models with individual carbon stars (see Papers II and III; Gautschi-Loidl et al. 2004; Nowotny et al. 2010; Sacuto et al. 2011).

Two types of systematic exceptions from the good overall agreement between models and observations should, however, be mentioned here: in various diagrams we note (a) groups of models with no observed counterparts, and (b) ranges of observed quantities not fully covered by models. Both phenomena can, in principle, be caused by the chosen range of parameters of the model grid, or by effects of intrinsic physical assumptions in the models. In particular, we find the following notable discrepancies: (i) our grid does not fully cover the extreme red end of the $(J-K)$ range in the Whitlock et al. (2006) sample, possibly because the highest mass-loss rates in the models are smaller than the highest values derived for that group of stars. In this context, we note that the value of the dust-to-gas ratio commonly assumed to derive mass-loss rates from observations (i.e. 0.005) is significantly higher than the typical values found in our models (cf. Fig. 5), and that the theoretical values show a large spread. (ii) Models combining low mass and low luminosity with high enough carbon excess and pulsation amplitude to initiate a wind have no counterparts among the observed stars in the diagrams showing mass loss vs. period or K magnitude vs. $(J-K)$. In addition, the models with the highest carbon excess used in this grid have a tendency to produce too high wind velocities compared with the bulk of observed stars. A major determining factor for the outflow velocity is the carbon excess, and thus the amount of amC grains formed. This leads us to conclude that stars with such high carbon excess are rare. (iii) In contrast to models at the high end of the assumed $(C-O)$ range, models that do form winds with the lowest $(C-O)$ values tend to show too low outflow velocities compared with their comparatively high mass-loss rates. Based on an exploratory study by

Mattsson & Höfner (2011), we expect that using size-dependent grain opacities (instead of the small particle limit) will increase the wind speeds of this model group without affecting the mass-loss rates significantly, bringing them into agreement with the bulk of the observed stars in the mass-loss rate vs. wind velocity diagram.

As a consequence of the present results, we plan to improve the modelling regarding both intrinsic model assumptions and parameter ranges. In particular, we will provide a full grid based on size-dependent grain opacities, which may both solve current problems with wind velocities, and probably improve synthetic V magnitudes, for example, for which the effects of dust are crucial. Then also smaller carbon excesses will be included in the parameter range of the grid, which is expected to bring the location of models with low or no mass loss in the $(J-H)$ vs. $(H-K)$ diagram into better agreement with observations.

Conclusions relevant for the *application of mass-loss rates in stellar evolution models* can be summarized as follows: the dynamic effects resulting from increasing the luminosity amplitude relative to the grid by Mattsson et al. (2010) by a factor of 2 for otherwise identical parameters (i.e. similar input of kinetic energy by pulsation) are small, both regarding the mass-loss rates and the outflow velocities. Moreover, as demonstrated in the exploratory study by Mattsson & Höfner (2011), using size-dependent grain opacities instead of the small-particle limit probably does not affect the mass-loss rates considerably (despite a noticeable effect on outflow speeds for slow winds). Some exceptions to these conclusions may apply to marginal winds (low velocity and low mass-loss rates), but these are not expected to have a significant effect on evolution models. Therefore we conclude that the mass-loss rates given by Mattsson et al. (2010) can be used for stellar evolution modelling, even in the light of current and pending improvements affecting synthetic spectra, photometry, and other observables derived from the models.

It should also be mentioned here that the mass-loss formula given by Wachter et al. (2002) (based on an older generation of dynamical wind models) gives systematically higher values of mass-loss rates for the same combinations of stellar parameters. In the light of the rather good agreement of our model grid with observations, mass-loss rates resulting from the Wachter et al. (2002) formula probably need to be revised downwards.

Acknowledgements. This research was funded by the Austrian Science Fund (FWF): P21988-N16, P23006, P23586. This work was supported by the Swedish Research Council. BA acknowledges funding by the contracts ASI-INAF I/016/07/0 and ASI-INAF I/009/10/0. This research has made use of (i) NASA's Astrophysics Data System, (ii) the VizieR catalogue access tool, CDS, Strasbourg, France, (iii) the SIMBAD database, operated at CDS, Strasbourg, France, and (iv) the NASA/IPAC Infrared Science Archive, which is operated by the Jet Propulsion Laboratory, California Institute of Technology, under contract with the National Aeronautics and Space Administration. This publication makes use of data products from the Two Micron All Sky Survey, which is a joint project of the University of Massachusetts and the Infrared Processing and Analysis Center/California Institute of Technology, funded by the National Aeronautics and Space Administration and the National Science Foundation. The computations were performed on resources provided by the Swedish National Infrastructure for Computing (SNIC) at UPPMAX. We thank the anonymous referee for the comments that helped improve the paper.

References

Aringer, B. 2000, PhD thesis, Univ. of Vienna
 Aringer, B., Girardi, L., Nowotny, W., Marigo, P., & Lederer, M. T. 2009, A&A, 503, 913 (Paper I)
 Asplund, M., Grevesse, N., & Sauval, A. J. 2005, in Astronomical Society of the Pacific Conference Series, Vol. 336, Cosmic Abundances as Records of Stellar Evolution and Nucleosynthesis, ed. T. G. Barnes, III & F. N. Bash, 25
 Bergeat, J., Knapik, A., & Rutily, B. 2001, A&A, 369, 178

Bertelli, G., Girardi, L., Marigo, P., & Nasi, E. 2008, A&A, 484, 815
 Bessell, M. S. 1990, PASP, 102, 1181
 Bessell, M. S. & Brett, J. M. 1988, PASP, 100, 1134
 Cherchneff, I. 2006, A&A, 456, 1001
 Cherchneff, I. 2012, A&A, 545, A12
 De Beck, E., Decin, L., de Koter, A., et al. 2010, A&A, 523, A18
 Feast, M. W., Glass, I. S., Whitelock, P. A., & Catchpole, R. M. 1989, MNRAS, 241, 375
 Gautschi-Loidl, R., Höfner, S., Jørgensen, U. G., & Hron, J. 2004, A&A, 422, 289
 Groenewegen, M. A. T., Sevenster, M., Spoon, H. W. W., & Pérez, I. 2002, A&A, 390, 511
 Groenewegen, M. A. T., Whitelock, P. A., Smith, C. H., & Kerschbaum, F. 1998, MNRAS, 293, 18
 Groenewegen, M. A. T., Baas, F., Blommaert, J. A. D. L., et al. 1999, A&AS, 140, 197
 Gullieuszk, M., Groenewegen, M. A. T., Cioni, M.-R. L., et al. 2012, A&A, 537, A105
 Gustafsson, B. & Höfner, S. 2003, in Asymptotic giant branch stars, by Harm J. Habing and Hans Olofsson. Astronomy and astrophysics library, New York, Berlin: Springer, 2003, p. 149, ed. H. J. Habing & H. Olofsson, 149
 Herwig, F. 2005, ARA&A, 43, 435
 Höfner, S., Gautschi-Loidl, R., Aringer, B., & Jørgensen, U. G. 2003, A&A, 399, 589
 Ita, Y., Tanabé, T., Matsunaga, N., et al. 2004, MNRAS, 353, 705
 Jura, M. 1987, ApJ, 313, 743
 Karakas, A. I. 2011, in Astronomical Society of the Pacific Conference Series, Vol. 445, Why Galaxies Care about AGB Stars II: Shining Examples and Common Inhabitants, ed. F. Kerschbaum, T. Lebzelter, & R. F. Wing, 3
 Knapp, G. R., Young, K., Lee, E., & Jorissen, A. 1998, ApJS, 117, 209
 Le Bertre, T. 1997, A&A, 324, 1059
 Marigo, P., Bressan, A., Nanni, A., Girardi, L., & Pumo, M. L. 2013, MNRAS, 434, 488
 Marigo, P., Girardi, L., Bressan, A., et al. 2008, A&A, 482, 883
 Mattsson, L. & Höfner, S. 2011, A&A, 533, A42
 Mattsson, L., Wahlin, R., & Höfner, S. 2010, A&A, 509, A14 (MWH10)
 Netzer, N. & Elitzur, M. 1993, ApJ, 410, 701
 Nowotny, W., Aringer, B., Höfner, S., & Eriksson, K. 2013, A&A, 552, A20 (Paper III)
 Nowotny, W., Aringer, B., Höfner, S., & Lederer, M. T. 2011, A&A, 529, A129 (Paper II)
 Nowotny, W., Höfner, S., & Aringer, B. 2010, A&A, 514, A35
 Ramstedt, S., Schöier, F. L., Olofsson, H., & Lundgren, A. A. 2008, A&A, 487, 645
 Sacuto, S., Aringer, B., Hron, J., et al. 2011, A&A, 525, A42
 Schöier, F. L. & Olofsson, H. 2001, A&A, 368, 969
 Stancliffe, R. J. & Lattanzio, J. C. 2011, in Astronomical Society of the Pacific Conference Series, Vol. 445, Why Galaxies Care about AGB Stars II: Shining Examples and Common Inhabitants, ed. F. Kerschbaum, T. Lebzelter, & R. F. Wing, 29
 Vassiliadis, E. & Wood, P. R. 1993, ApJ, 413, 641
 Wachter, A., Schröder, K.-P., Winters, J. M., Arndt, T. U., & Sedlmayr, E. 2002, A&A, 384, 452
 Whitelock, P. A., Feast, M. W., Marang, F., & Groenewegen, M. A. T. 2006, MNRAS, 369, 751 (W06)
 Wood, P. R., Alcock, C., Allsman, R. A., et al. 1999, in IAU Symposium, Vol. 191, Asymptotic Giant Branch Stars, ed. T. Le Bertre, A. Lebre, & C. Waelkens, 151

Appendix A: Details on the representative cases

In Sect. 3 we defined different classes of time-dependent behaviour and illustrated them with the help of selected models, as shown in Fig. 1. While we kept the stellar mass ($0.75 M_{\odot}$) and the f_L parameter (2) fixed for this group of models, the other parameters varied as listed in Table A.1. The models are labelled as $T_{\star}/\log(L_{\star})/M_{\star}/\log(C-O)+12/\Delta u_p/f_L$ with L_{\star} and M_{\star} in solar units.

The photometric amplitudes and other properties for the illustrative cases can also be found in Table A.1. The column A_V^{CSE} gives the extinction in the V band (at $0.55 \mu\text{m}$) at the phase 0.25 (or, more precisely, the mean of these values for all computed cycles); as is further discussed in Paper III, this is a measure of the lower limit of the dust extinction in the model.

Table A.1. Model parameters and resulting photometric properties of the representative cases plotted in Fig. 1. The Δm_{bol} , ΔK and ΔV columns give the mean amplitude over the computed cycles of the bolometric, K - and V -band radiation (in magnitudes), whereas the “ V -range” column gives the full range of V -band variations (cycle-to-cycle variations). The column labelled A_V^{CSE} gives the typical optical depth in the V band at bolometric phase 0.25 (see text). The typical positions in the two-colour ($J-H$) vs. ($H-K$) diagram are also given.

class	model $T_\star / \log(L_\star) / M_\star / \log(C-O) + 12 / \Delta u_p / f_L$	Δm_{bol} [mag]	ΔK [mag]	ΔV [mag]	A_V^{CSE} [mag]	V -range [mag]	$(H-K)$, $(J-H)$ [mag], [mag]
<i>pp</i>	3000/3.55/0.75/8.50/2/2.0	0.38	0.42	0.72	0.00	0.72?	0.53, 0.92
<i>pm</i>	2800/3.55/0.75/8.50/2/2.0	0.34	0.40	0.84	0.05	0.84?	0.58, 0.91
<i>pn</i>	2600/3.70/0.75/8.20/4/2.0	0.69	0.68	1.33	0.56	2.34	0.6–0.9, 0.7–1.2
<i>we</i>	2800/3.85/0.75/8.20/6/2.0	1.42	1.48	2.37	2.71	4.67	0.9–1.4, 0.9–1.8
<i>ws</i>	2800/3.85/0.75/8.50/2/2.0	0.45	0.43	0.69	1.82	1.00	0.91, 1.25
<i>wp</i>	2800/3.70/0.75/8.80/4/2.0	0.81	0.84	3.78	2.98	4.46	1.1–1.4, 1.3–1.8
<i>wn</i>	2800/3.70/0.75/8.80/6/2.0	1.26	1.53	6.71	4.55	8.94	1.2–1.8, 1.8–2.4

pp: 3000/3.55/0.75/8.50/2/2.0

In this particular case, the largest extension is 1.5 stellar radii. No dust is formed in this model, the light curves show a very regular and repeated variation from cycle to cycle; the amplitudes (maximum-to-minimum) are 0.38^{mag} , 0.42^{mag} and 0.72^{mag} for the bolometric, K and V magnitudes. It has the position (0.53, 0.92) in the ($J-H$) vs. ($H-K$) two-colour-diagram.

pm: 2800/3.55/0.75/8.50/2/2.0

This model has the same parameters as the *pp* one except that it is 200 K cooler. It is classified as *pm* and shows a different dynamic behaviour where the outer boundary varies from smallest to largest extension and back in almost precisely two luminosity periods. The largest extension of the atmosphere is about $2 R_\star$; it extends to $\geq 2 R_\star$ every fourth (luminosity) cycle interleaved with an expansion to $\lesssim 2 R_\star$ (also every fourth cycle). This behaviour is coupled to a higher dust condensation every fourth cycle when the stellar material reaches greater heights. We can note that although the condensation degree is lower than 10^{-3} , the influence of the dust on the photometric behaviour is clearly visible. The amplitudes are 0.34^{mag} , 0.40^{mag} and 0.84^{mag} for the bolometric, K and V magnitudes, respectively, where we note that the amplitude in V has increased (from the previous *pp* model) because of the dust. The minima (and maxima) are fainter in the presence of dust a distance, r , $\sim 1.5 - 2 R_\star$. [It might be classified as a SRa type variable star.] Its position in the ($J-H$) vs. ($H-K$) diagram is at (0.58, 0.91), that is, slightly redder in ($H-K$) than the previous one.

pn: 2600/3.70/0.75/8.20/4/2.0

Compared with the *pm* model, it has a lower T_\star by 200 K and an increased luminosity, and also an increased piston velocity amplitude but a lower carbon excess. Here the pulsations cause the atmosphere to expand to between 2 and $4 R_\star$ in a rather irregular way. The condensation degree varies from a few percent up to about 25% without any obvious correlation to the pulsation behaviour of the atmosphere. Now we see a stronger influence of dust on the photometric properties. The amplitudes of the variation in bolometric, K and V magnitudes are 0.69^{mag} , 0.68^{mag} and 1.33^{mag} (if we take the mean over all computed cycles; the maximum-to-minimum variation in V over the computed range is 2.34^{mag}). [It might be classified as a mira variable.] This model

is situated around (0.6–0.9, 0.7–1.2) in a ($J-H$) vs ($H-K$) plot, that is, redder than the *pm* model, especially in ($H-K$).

we: 2800/3.85/0.75/8.20/6/2.0

This model is 200 K warmer than the *pn* one, but with increased luminosity and piston velocity amplitude. This model rarely has an atmospheric extension smaller than $5 R_\star$. The condensation degree varies between 5 and 30%, which implies quite a strong effect on the photometric properties. The amplitudes for the bolometric, K and V magnitudes are 1.42^{mag} , 1.48^{mag} and 2.37^{mag} (the total range in V over all the computed cycles is 4.67^{mag}). [It might be classified as a mira variable during its wind phase.] In the two-colour ($J-H$) vs ($H-K$) diagram the model occupies the range 0.9–1.4 in ($H-K$) and 0.9–1.8 in ($J-H$); compared with the *pn* model, it has moved along the blackbody line towards cooler temperatures.

ws: 2800/3.85/0.75/8.50/2/2.0

This model has the same temperature and luminosity as the *we* model, but a higher carbon excess, so it develops a wind even at the low piston amplitude of $\Delta u_p = 2 \text{ km s}^{-1}$. It has a dust condensation degree that is almost constant in time, at $15 \pm 1\%$. The amplitudes in the bolometric, K and V magnitudes are 0.45^{mag} , 0.43^{mag} and 0.69^{mag} , respectively, (the total range in V over all the computed cycles is 1.00^{mag}). Its position in the ($J-H$) vs. ($H-K$) diagram is at (0.91, 1.25) with a small variation since the amount of dust is almost constant.

wp: 2800/3.70/0.75/8.80/4/2.0

A model with a lower luminosity than our *we* case but a higher carbon excess and piston velocity amplitude, it has a wind in which dust condenses at $r \sim 1.5 R_\star$ every cycle around phase 0.5. The photometric amplitudes are 0.81^{mag} , 0.84^{mag} and 3.78^{mag} for the bolometric, K and V magnitudes (the total range in V over all the computed cycles is 4.46^{mag}). [It might certainly be classified as a mira variable.] The dust condensing around phase 0.5 makes the minima in V quite deep. In the two colour diagram the model varies (loops), along the blackbody line, between 1.1–1.4 in ($H-K$) and between 1.3–1.8 in ($J-H$).

wn: 2800/3.70/0.75/8.80/6/2.0

It has the same parameters as the *wp* case, but a higher piston velocity amplitude. Here the wind is more irregular, the dust is still formed around $r \sim 1.5 R_\star$ but in a more irregular fashion. The amplitudes in the bolometric, K and V magnitudes are 1.26^{mag} , 1.53^{mag} and 6.71^{mag} , respectively, (the total range in V over all the computed cycles is 8.94^{mag}). In the two-colour diagram the model moves during the pulsations along the blackbody line between 1.2–1.8 in $(H - K)$ and between 1.8–2.4 in $(J - H)$.

Appendix B: Model overview

In the following pages we present a table with photometric and dynamic properties of the models in the present grid. The models are arranged in increasing effective temperature, luminosity, and stellar mass. For each such combination the data are ordered by increasing carbon excess, piston velocity amplitude, and f_L . In each line, after the model parameters we list the assigned class, $\log g$ (surface gravity in cgs units). Then come dynamic quantities evaluated at the outer boundary: mass-loss rate (in solar masses per year), the wind velocity (km/s), the carbon condensation degree, and the dust-to-gas ratio. Note that all given values are temporal means, see Sect. 2.3. Then follow the photometric properties: the (full) amplitude of the bolometric magnitude, the mean V magnitude, the range of V magnitudes, the mean K magnitude and its range, and finally the colours ($V-I$), ($V-K$), ($J-H$) and ($H-K$).

The luminosities and stellar masses are given in solar units. The carbon excesses, $\log(C-O)+12$ are given on the scale where $\log N_H \equiv 12.00$. The piston velocity amplitudes, Δu_p , are given in km/s. The f_L and class designations are described in Sect. 2.2 and Sect. 3 respectively. All the photometric quantities are given in magnitudes.

Appendix C: Material at the CDS

The resulting spectra and synthetic photometric magnitudes in various filters are available for downloading, some photometric data are also summarized in Table B.1 along with dynamic data, such as mass-loss rates and wind velocities.

Among the downloadable material there is also, for each individual model, a two-page fact sheet that looks like Figs. C.1 and C.2 summarizing the dynamic and photometric behaviour. It should be noted that the values for mass-loss rates, gas velocities, and carbon condensation degrees plotted on the fact sheets are values for each snapshot, whereas the values for these quantities given in the figures and tables in this article are computed as averages over pulsation periods as described in Sect. 2.3.

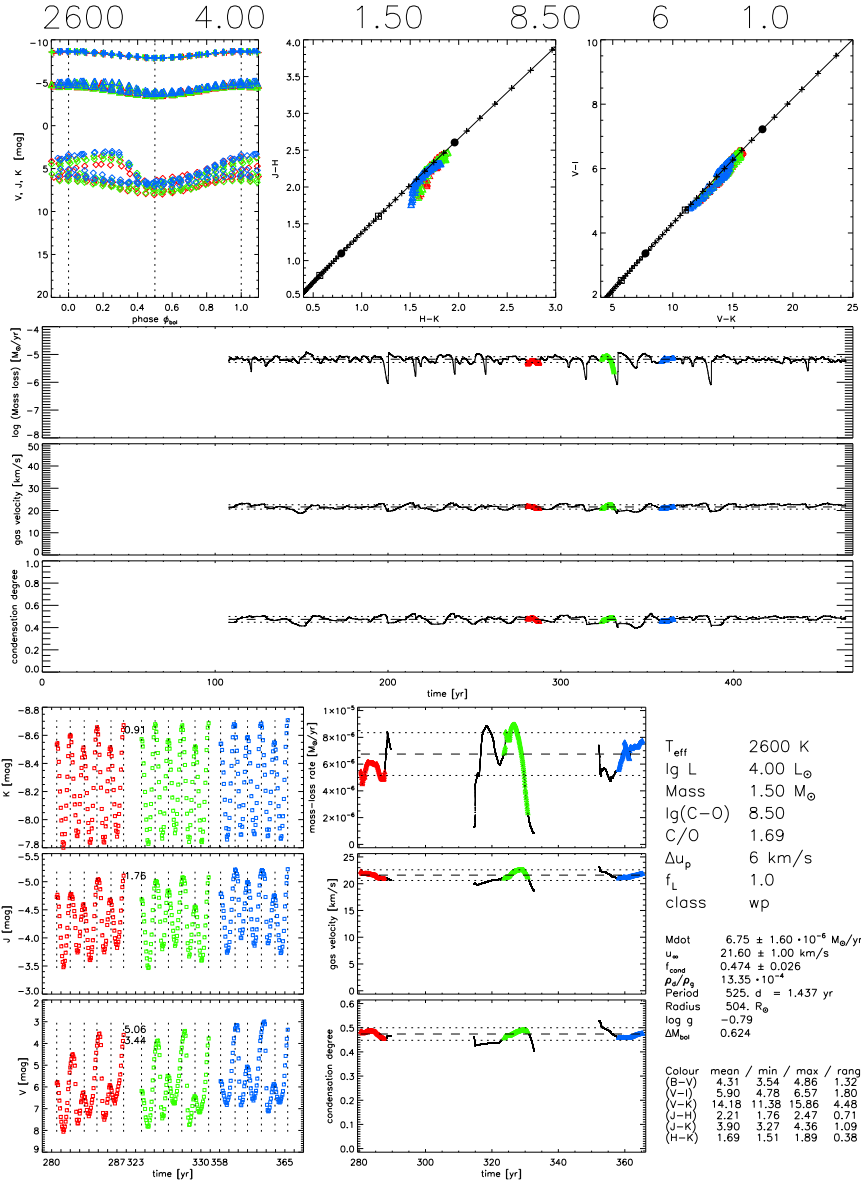


Fig. C.1. Example of the first page of the fact sheets. The top label gives T_{\star} , $\log L_{\star}$, M_{\star} , $\log(C-O)+12$, Δu_p , and f_L for a quick overview. The upper leftmost diagram gives the K , J and V magnitudes as a function of phase (with maximum luminosity at phase 0.0). The ranges are identical on all fact sheets to facilitate comparisons of different models; this is true for the three upper diagrams. The different colours correspond to the different epochs selected for the spectral synthesis. The middle and right upper panels show two colour-colour diagrams, the blackbody line is also shown. The three middle panels show, as a function of time, the mass-loss rate, the gas velocity, and the condensation degree for carbon, all three at the outer boundary ($25 R_{\star}$); here the vertical scales are identical on all fact sheets, the time intervals do vary from model to model. For the models without a wind, the position of the outer boundary is shown instead of the mass-loss rate. For the episodic models, we show both of them. The horizontal dashed and dotted lines denote the mean value, and the mean value \pm the standard deviation. The bottom part contains the light-curves in K , J and V ; here the dotted vertical lines denote the positions of the luminosity maxima, the maximum range in magnitudes is also given, for the V magnitude also the mean amplitude over a (luminosity) cycle. Enlarged versions of the three middle plots, now with automatic scaling, are shown for the selected epochs. Finally, a summary of parameters, dynamic and photometric properties are listed.

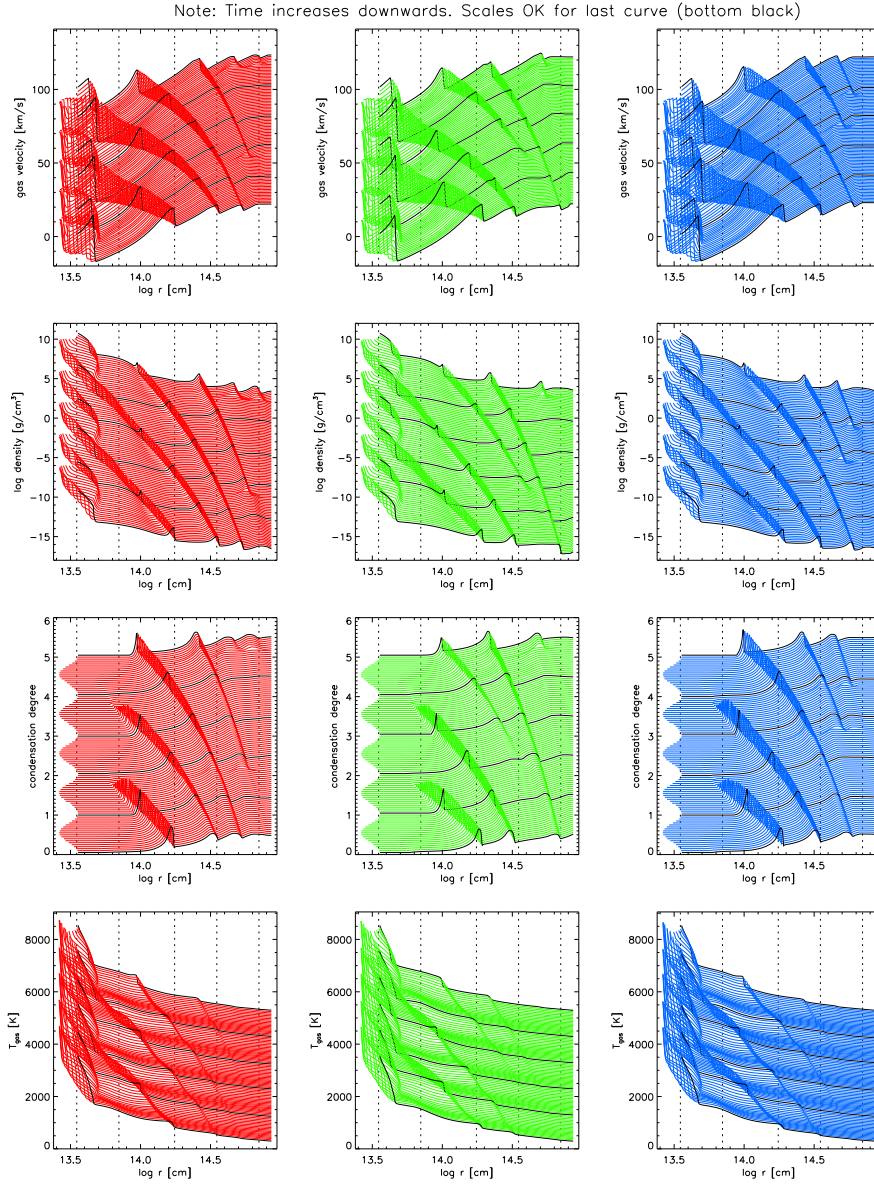


Fig. C.2. Example of the second page of the fact sheets. The colours in the plots correspond to the selected epochs as given on the first page. In each column we show, from top to bottom, the gas velocity, density, carbon condensation degree, and gas temperature, all as a function of distance from the stellar centre. In each panel, individual curves correspond to snapshots in time, and time increases downwards. The distance between two curves is approximately 0.05 in phase. The curves closest in time to phase 0.0 are drawn with thick black lines. The ordinate scales apply to the bottom (last) curve. The vertical short-dashed lines in the panels denote the distances 1, 2, 5, 10, and 20 stellar radii.